








Cite this: *Phys. Chem. Chem. Phys.*,  
2021, **23**, 14889

# Influence of the Pd : Bi ratio on Pd–Bi/Al<sub>2</sub>O<sub>3</sub> catalysts: structure, surface and activity in glucose oxidation†

Mariya P. Sandu, <sup>ab</sup> Mikhail A. Kovtunov, <sup>a</sup> Vladimir S. Baturin, <sup>cd</sup>  
Artem R. Oganov <sup>e</sup> and Irina A. Kurzina <sup>\*a</sup>

Pd–Bi nanoparticles show high efficiency in catalyzing gluconic acid production by the glucose oxidation reaction. Although this type of catalyst was studied for some time, the correlation between bismuth content and catalytic activity is still unclear. Moreover, there is little information on the principles of the formation of Pd–Bi nanoparticles. In this work, the relation between bismuth content and the activity and selectivity of the Pd<sub>x</sub>Bi<sub>y</sub>/Al<sub>2</sub>O<sub>3</sub> catalyst in the glucose oxidation process was studied. The catalytic samples were prepared by co-impregnation of the alumina support utilizing the metal–organic precursors of Pd and Bi. The samples obtained were tested in the glucose oxidation reaction and were studied by transmission electron microscopy (TEM), X-ray fluorescence analysis, X-ray photoelectron spectroscopy (XPS), and BET adsorption. It has been found that the Pd<sub>3</sub>:Bi<sub>1</sub> atomic ratio grants the highest catalytic efficiency for the studied samples. To explain this, we predicted stable Pd–Bi nanoparticles using *ab initio* evolutionary algorithm USPEX. The calculations demonstrate that nanoparticles tend to form Pd(core)–Bi(shell) structures turning to a crown-jewel morphology at lower Bi concentration, thus exposing the active Pd centers while maintaining the promoting effect of Bi.

Received 24th March 2021,  
Accepted 14th June 2021

DOI: 10.1039/d1cp01305j

[rsc.li/pccp](http://rsc.li/pccp)

## Introduction

Gluconic acid and its derivatives are valuable products of glucose oxidation, which are used in various branches of industry and everyday life due to their low toxicity, low corrosive activity and ability to create complex compounds, used as detergents, food additives and drugs.<sup>1,2</sup> Biotechnological synthesis, which currently dominates the industry, is based on the fermentation of a glucose containing substrate by various bacterial strains and makes it possible to produce gluconic acid with high efficiency.<sup>3,4</sup> This method, however, possesses significant drawbacks. The reaction medium must be extremely sterile before strain transfer and friendly for bacterial metabolism,<sup>5,6</sup> the fermentation process lasts relatively long

(usually up to 100 hours),<sup>7,8</sup> and the product recovery presents a challenging task.<sup>9,10</sup> Also, microorganisms are very susceptible to any kind of mechanical stress, which can reduce the productivity of a strain and even lead to its death in the reactor.<sup>11</sup>

Heterogeneous catalysis is free of all the above mentioned drawbacks and allows reaching high yield and selectivity of the reaction.<sup>12–15</sup> Currently, bimetallic catalysts are attracting significant attention due to their high efficiency and stability in this reaction.<sup>16–18</sup> In particular, it was shown that the glucose conversion achieved on monometallic catalysts was 10% for Pt/C and 15% for Au/C, while bimetallic catalysts made it possible to get vastly better values – 80% for Au–Pt without a support and 90% for Au–Pt/C.<sup>16</sup> The greater activity, selectivity, and stability of such catalysts are probably due to the electronic interaction between metals' atoms, as a result of which the promoter creates an excess of electron density on the active component's atoms.<sup>19,20</sup> The presence of a modifier may also decrease the energy of adsorption of the reagents on the active component, which easily returns the active sites to an unoccupied state,<sup>21</sup> thus preventing poisoning of the catalysts.

Among the bimetallic catalysts described in the literature, catalytic samples based on palladium promoted with bismuth are highly efficient, since the promoting effect of the latter on palladium leads to extremely high gluconic acid yields and reaction selectivity.<sup>22–25</sup> Studies<sup>25–27</sup> indicate a gluconic acid

<sup>a</sup> National Research Tomsk State University, Prospekt Lenina, 36, 634050, Tomsk, Russia. E-mail: [kurzina99@mail.ru](mailto:kurzina99@mail.ru)

<sup>b</sup> Siberian State Medical University, Moskovsky Tract, 2, 634050, Tomsk, Russia

<sup>c</sup> Vernadsky Institute of Geochemistry and Analytical Chemistry of Russian Academy of Sciences, Kosygina, 19, Moscow, 119991, Russia

<sup>d</sup> I. E. Tamm Theory Department, Lebedev Physical Institute, Russian Academy of Sciences, Leninskii Prospekt, 53, Moscow, 119991, Russia

<sup>e</sup> Skolkovo Institute of Science and Technology, Bolshoy Boulevard, 30, Building 1, 121205, Moscow, Russia

† Electronic supplementary information (ESI) available. See DOI: 10.1039/d1cp01305j

yield of more than 98% and a selectivity of more than 97% on the 2Pd:Bi1/C, Pd10:Bi1/C, and 2.8 Pd–Bi1/C catalysts. For catalysts of this composition, it is important to select the optimal stoichiometric ratio of palladium and bismuth that would make it possible to find a balance between activity, cost, and stability of the sample in several reaction steps. However, there is practically no systematic research of these systems that would elucidate simultaneously the interconnection of their structural, electronic, and catalytic features. Thus, in this work we will attempt to explain the catalytic performance of Pd<sub>x</sub>:Bi<sub>y</sub>/Al<sub>2</sub>O<sub>3</sub> samples based on the surface electronic properties and structural organisation.

In this work the influence of the Pd:Bi atomic ratio on the catalytic activity of five Pd<sub>x</sub>:Bi<sub>y</sub>/Al<sub>2</sub>O<sub>3</sub> samples prepared using metal–organic precursors was investigated in the selective glucose oxidation reaction. The measurements show that the highest conversion is achieved at a rather low fraction of bismuth (Pd3:Bi1 and Pd5:Bi2). To investigate this trend, the structural features of the catalyst were modelled using first principles evolutionary calculations. We show that at lower bismuth concentrations, Pd<sub>n</sub>Bi<sub>m</sub> clusters possess the crown-jewel geometry with Bi atoms playing the role of “jewels”, turning into a core–shell morphology at a higher amount of bismuth. This result as well as the charge distribution between surface Pd and Bi atoms explains the measured catalytic behaviour with varying Pd:Bi ratios.

## Materials and methods

### Synthesis of catalytic samples

Microspherical  $\gamma$ -Al<sub>2</sub>O<sub>3</sub> (“SKTB Katalizator”) with diameters of 0.125–0.250  $\mu\text{m}$  and surface area of 174  $\text{m}^2 \text{g}^{-1}$  was used as a support. The total pore volume of the support was 0.35  $\text{cm}^3 \text{g}^{-1}$ .

Two monometallic Pd/Al<sub>2</sub>O<sub>3</sub> and Bi/Al<sub>2</sub>O<sub>3</sub> and five bimetallic Pd<sub>x</sub>:Bi<sub>y</sub>/Al<sub>2</sub>O<sub>3</sub> samples were synthesized in the work. For bimetallic samples different values of Pd:Bi atomic ratio have been chosen: 1:2, 1:1, 2:1, 5:2, and 3:1. Catalysts were prepared according to the procedure described in ref. 28.

### Texture characterization

The surface area, average pore size and total pore volume of the obtained samples were determined using a TriStar 3020 analyser (Micromeritics, USA). Approximately 100 mg of each sample were degassed for 2 hours using VacPrep 061 (Micromeritics, USA) before measurement. A Brunauer–Emmett–Teller method was implemented for surface area value calculation, and a Barrett–Joyner–Halenda method was used for pore size and pore volume determination.

### X-ray fluorescence analysis (XRF)

Elemental analysis of the samples was performed with an X-ray fluorescence spectrometer Lab Center XRF-1800 (Shimadzu, Japan). The X-ray tube with 40 kV voltage, 95 mA amperage, and aperture of 3 mm was used for qualitative and quantitative analysis. An X-ray generator was presented by a Rh-anode with a

power of 4 kW. Measurement was conducted at a scanning step of 8 degree  $\text{min}^{-1}$ . The device error was 10%.

### Transmission electron microscopy (TEM)

The morphology, particle size distribution and local chemical composition of nanoparticles were determined by transmission electron microscopy (TEM) and energy dispersive spectrometry (EDS). We used JEOL JEM-2100F (JEOL Ltd, Akishima, Tokyo, Japan) operating at 200 kV, equipped with an electron gun with field emission of the cathode (FEG), a high-resolution pole tip (with a point resolution of 0.19 nm) and a JEOL JED-2300 Analysis Station spectrometer (JEOL Ltd, Akishima, Tokyo, Japan).

### X-ray photoelectron spectroscopy (XPS)

The surface of the catalysts was studied by XPS. The measurements were carried out using a PHI 5000 VersaProbe-II (ULVAC-PHI, Chigasaki, Kanagawa, Japan) spectrometer equipped with argon and electron guns for charge neutralization (double beam charge neutralization method). The Al 2p line was taken as an internal standard at 74.5 eV. The accuracy of the binding energy measurements was  $\pm 0.1$  eV for all the samples. The deconvolution of XPS peaks was carried out by a mixed Gaussian–Lorentzian correspondence by simultaneously subtracting the background caused by secondary electrons and photoelectrons losing energy, according to the Shirley algorithm. The XPS spectra were processed using standard CasaXPS software (Version 2.3.22 PR1.0, 2018, Casa Software Ltd, UK).

### Measurement of catalytic properties

Liquid phase oxidation of glucose was performed in the temperature range of 20–60  $^{\circ}\text{C}$ , at atmospheric pressure and in the pH range of 6–12 in a static quartz reactor. Also, the reaction was conducted without pH control. The pH level was maintained by supplying alkali and controlled using a glass combined electrode throughout the entire catalytic process. Glucose suspension (3.1 g) was previously dissolved in the reactor in 25 mL of water. Then the required amount of the catalyst was added, and the pH was adjusted to 9 by adding the required amount of 3 M NaOH (LenReactiv, Russia, 99%). Oxygen was supplied into the reaction medium at a flow rate of 10  $\text{mL min}^{-1}$ . The reaction was conducted for 150 min with continuous stirring (1000 rpm). Samples of the reaction mixture with a volume of 700  $\mu\text{l}$  were taken periodically for HPLC analysis. Glucose conversion ( $\bar{X}$ ), selectivity towards gluconic acid ( $S$ ), and its yield ( $Y$ ) were calculated afterwards based on the obtained HPLC data.

### HPLC analysis

For qualitative and quantitative determination of reaction products the column Zorbax NH2 250  $\times$  4.6 mm, 5  $\mu\text{m}$  (Agilent, USA) with a refractive index detector was used. The temperature of the column was kept at +55  $^{\circ}\text{C}$ . Silica gel with a bonded aminopropylsilane phase was used as a stationary phase. For the mobile phase a mixture of phosphate buffer solution

(pH 2.5) and acetonitrile was used (volume ratio of 1:3). Injection volume was 100  $\mu\text{L}$ .

### Pd<sub>x</sub>Bi<sub>y</sub> nanocluster structure optimization

Prediction of stable Pd<sub>n</sub>Bi<sub>m</sub> clusters ( $n \leq 20$ ,  $m \leq 15$ ) was performed using a variable-composition cluster structure prediction method<sup>29</sup> using the USPEX evolutionary code.<sup>30,31</sup> The total energy calculations and structure relaxations were performed using the projector augmented wave method<sup>32</sup> at the level of the generalized gradient approximation<sup>33</sup> as implemented in the VASP code.<sup>34,35</sup> In these calculations we used the plane wave kinetic energy cutoff of 450 eV, and to model finite systems the supercell method was used, where periodic images of a nanocluster are separated by a sufficient vacuum layer (12 Å) so that the interaction between periodic images vanishes. Bader partial atomic charges were calculated using the Multiwfn software.<sup>36</sup>

## Results and discussion

### Texture characterization

The specific surface area decreased by 34–47 m<sup>2</sup> g<sup>-1</sup> compared to the initial specific surface area of the support. Total pore volume remains unchanged for Pd5:Bi2, and other samples demonstrate a decrease by 0.02–0.09 cm<sup>3</sup> g<sup>-1</sup>. Texture characteristics among the prepared samples are practically identical. The lowest surface area, pore volume and pore size are attributed to the Pd1:Bi2/Al<sub>2</sub>O<sub>3</sub> sample. Exact values of the texture parameters are presented in the ESI,<sup>†</sup> Table S1.

### X-ray fluorescence analysis (XRF)

Table 1 shows the Pd and Bi percentage for all prepared samples obtained by XRF. Pd:Bi atomic ratio values calculated from XFA-data are 2.86, 2.40, 2.13, 1.05, and 0.55 for Pd3:Bi1, Pd5:Bi2, Pd2:Bi1, Pd1:Bi1, and Pd1:Bi2, respectively. The ratio for Pd3:Bi1/Al<sub>2</sub>O<sub>3</sub> and Pd5:Bi2/Al<sub>2</sub>O<sub>3</sub> are slightly below the required value, but in general actual atomic ratios are close to the desired ones.

### Transmission electron microscopy (TEM)

The surface of the catalysts was examined by TEM. TEM images are shown in Fig. 1, the lognormal particle size distributions are shown in Fig. 2. The Pd/Al<sub>2</sub>O<sub>3</sub> sample demonstrates a uniform distribution of nearly spherical metal particles over the support surface, the degree of particle aggregation is small, their diameter varies mainly from 1 to 8 nm, and the average diameter is 4.3 nm. Similar characteristics are obtained for Pd3:Bi1. A further increase of Bi content leads to greater average diameter (up to 14.5 nm), uneven particle distribution across the support surface and appearance of large aggregates reaching 45 nm in the case of Pd1:Bi2. This is due to the fact that the melting point of bismuth is 271 °C<sup>37</sup> and the addition of significant amounts of bismuth can lead to the sintering of particles at high temperatures (350–500 °C) during sample preparation. TEM-images for Bi/Al<sub>2</sub>O<sub>3</sub> (ESI,<sup>†</sup> Fig. S1) demonstrate

Table 1 Pd and Bi mass percentage in the obtained samples

Sample	Pd content, mass%	Bi content, mass%
Pd/Al <sub>2</sub> O <sub>3</sub>	1.3	—
Bi/Al <sub>2</sub> O <sub>3</sub>	—	2.0
Pd3:Bi1/Al <sub>2</sub> O <sub>3</sub>	3.5	2.4
Pd5:Bi2/Al <sub>2</sub> O <sub>3</sub>	2.8	2.3
Pd2:Bi1/Al <sub>2</sub> O <sub>3</sub>	2.5	2.3
Pd1:Bi1/Al <sub>2</sub> O <sub>3</sub>	2.3	4.3
Pd1:Bi2/Al <sub>2</sub> O <sub>3</sub>	1.1	3.9

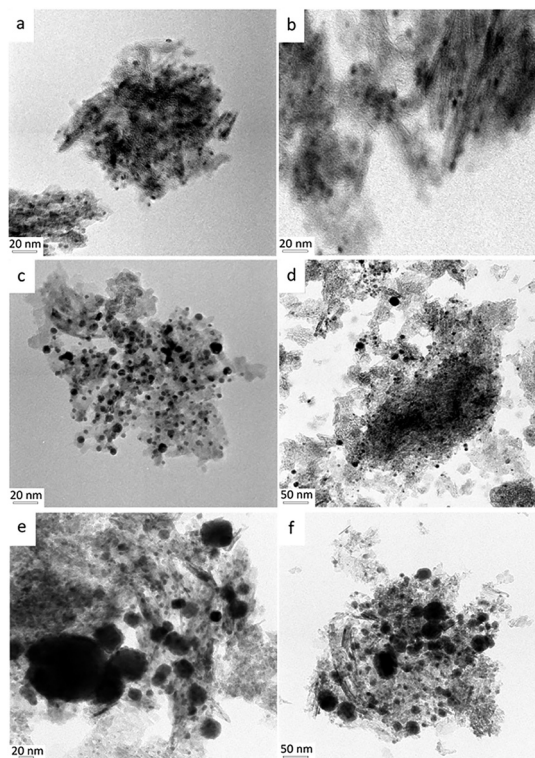


Fig. 1 TEM-images of Pd (a), Pd3:Bi1 (b), Pd5:Bi2 (c), Pd2:Bi1 (d), Pd1:Bi1 (e), and Pd1:Bi2 (f) samples.

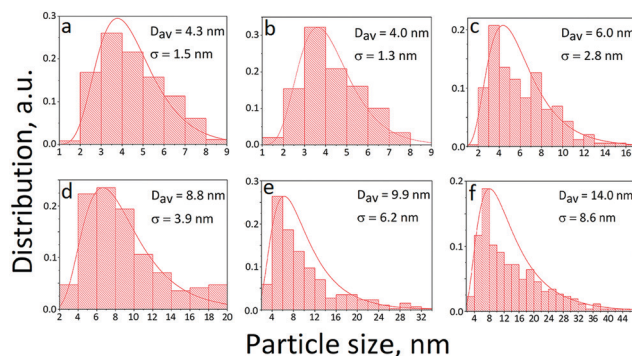


Fig. 2 Particle size distribution of Pd (a), Pd3:Bi1 (b), Pd5:Bi2 (c), Pd2:Bi1 (d), Pd1:Bi1 (e), and Pd1:Bi2 (f) samples supported by Al<sub>2</sub>O<sub>3</sub>.

large particle agglomerates of 170–450 nm. A distinct feature of the particle morphology for 30–45 nm particles is that their shape differs from spherical and resembles cuboctahedra. This shape of



nanoparticles indicates their formation from the smallest particles during the sintering of molten bismuth with palladium, provided that the rates of crystallization and growth of nuclei are comparable. Despite the contribution of these large particles, the histogram maximum remains under 10 nm. Therefore, the utilized synthesis method is suitable for obtaining nanoscale particles.

### X-ray photoelectron spectroscopy (XPS)

X-ray photoelectron spectroscopy (XPS) was used for investigation of the surface state for mono- and bimetallic samples (Fig. 3). Peak deconvolution was performed for pattern interpretation. XPS-patterns for Pd/Al<sub>2</sub>O<sub>3</sub> consists of two peaks related to Pd 3d<sub>3/2</sub> and Pd 3d<sub>5/2</sub> states with a binding energy of 340.7 eV and 335.2 eV, respectively. In the XPS profile for the Pd 3d<sub>5/2</sub> core-level, Pd<sup>0</sup> and Pd(II)<sub>ads</sub> phases are detected at 335.5 eV and 336.4 eV, respectively (Table 2).<sup>38,39</sup> The XPS pattern for the Bi 4f<sub>7/2</sub> core-level of Bi/Al<sub>2</sub>O<sub>3</sub> consists of two peaks related to Bi<sup>0</sup> and Bi(III)<sub>ads</sub> states with a binding energy of 156.8 eV and 158.0 eV, respectively.<sup>40,41</sup> The presence of oxidized phases is due to strong palladium and bismuth adsorption by the alumina surface during the synthesis.<sup>42</sup>

The XPS profile for Pd5 : Bi2 demonstrates peak shifts for Pd 3d<sub>5/2</sub> and Bi 4f<sub>7/2</sub> core-levels. Peaks previously attributed to the Pd<sup>0</sup> and Pd(II)<sub>ads</sub> are now located at 334.5 and 336.3, respectively. Peaks associated with Bi<sup>0</sup> and Bi(III)<sub>ads</sub> states are located at 156.6 and 158.7, respectively. The peaks for Pd(II) and Bi<sup>0</sup>

Table 2 Binding energies (in eV) for Pd 3d<sub>5/2</sub> and Bi 4f<sub>7/2</sub> core-levels

Sample	Pd 3d <sub>5/2</sub>	Bi 4f <sub>7/2</sub>
Pd	Pd <sup>0</sup> 335.2, Pd(II) <sub>ads</sub> 336.4	—
Bi	—	Bi <sup>0</sup> 156.8 Bi(III) <sub>ads</sub> 158.0
Pd3 : Bi1	Pd <sup>0</sup> 334.6 Pd(II) <sub>ads</sub> 336.0	Bi <sup>0</sup> 156.5 Bi(III) <sub>ads</sub> 158.2
Pd5 : Bi2	Pd <sup>0</sup> 334.5 Pd(II) <sub>ads</sub> 336.3	Bi <sup>0</sup> 156.6 Bi(III) 158.7
Pd2 : Bi1	Pd <sup>0</sup> 334.6 Pd(II) <sub>ads</sub> 336.1	Bi <sup>0</sup> 157.1 Bi(III) <sub>ads</sub> 158.4
Pd1 : Bi1	Pd <sup>0</sup> 334.4 Pd(II) <sub>ads</sub> 336.2	Bi <sup>0</sup> 157.1 Bi(III) <sub>ads</sub> 158.3
Pd1 : Bi2	Pd <sup>0</sup> 334.4 Pd(II) <sub>ads</sub> 336.2	Bi(III) <sub>ads</sub> 157.6 Bi(III) 158.7

states change their position only slightly (0.1 and 0.2 eV, respectively), while the shift for Pd<sup>0</sup> and Bi(III)<sub>ads</sub> is significantly larger (0.7 eV). One can assume that electron transfer to Pd<sup>0</sup> from bismuth adsorbed by alumina oxygen or palladium takes place.<sup>43</sup> It arises due to strong metal interaction created at the heat treatment stage.<sup>44,45</sup> Apparently, in this case Bi(III)<sub>ads</sub> undergoes full oxidation and yields the Bi(III) phase. The Pd3 : Bi1 sample shows no appreciable peak shifts for Bi 4f<sub>7/2</sub>. Palladium states still seem to be affected by the presence of bismuth, which results in Pd<sup>0</sup> and Pd(II)<sub>ads</sub> peak displacement (0.6 and 0.4 eV, respectively), but the bismuth content is insufficient to create bismuth-associated peak shifts.

For the Pd1 : Bi2 sample, significant peak displacement is noted for the Pd<sup>0</sup>, Bi<sup>0</sup>, and Bi(III) states. Again, as shown before for the Pd5 : Bi2 sample, a peak attributed to Bi(III)<sub>ads</sub> is shifted to 158.7 eV, which is likely to be indicative of Bi(III) state formation. Simultaneously, a peak associated with Bi<sup>0</sup> also changes its position. Thus Bi(III)<sub>ads</sub> and Bi<sup>0</sup> are responsible for electron transfer to Pd<sup>0</sup>. There is still a noticeable difference (0.4 eV) between the Bi(III)<sub>ads</sub> peak for the monometallic sample and the shifted peak for Bi<sup>0</sup> of the Pd1 : Bi2 sample. A complete absence of Bi<sup>0</sup> is possible since EDX-analysis shows the excess of oxygen in this sample (ESI,† Table S2). Bismuth's higher affinity to oxygen and its deposition over the palladium core create suitable conditions for bismuth to adsorb the majority of oxygen atoms. Presumably, Bi<sup>0</sup> is not oxidized to Bi(III), but has an intermediate oxidation state typical for alloys. The same tendency is observed for Pd2 : Bi1 and Pd1 : Bi1 samples.

Bader partial charge analysis performed on a stable structure of Pd–Bi nanoclusters shows that the intermetallic interaction leads to the excess of electron density on palladium atoms created by intermetallic electron transfer (−0.25 elementary charge on Pd and +0.41 – on Bi, see the ESI,† Table S3 for more details). This must significantly enhance the catalytic performance of the bismuth-promoted samples compared to Pd/Al<sub>2</sub>O<sub>3</sub>. In particular, it must facilitate glucose adsorption through hydrogen since it is characterized by a partial positive charge induced by the oxygen in glucose. At the same time, a negative peak shift is observed among Pd<sub>x</sub>:Bi<sub>y</sub> samples with particle growth (334.6, 334.5, and 334.4 eV for Pd3 : Bi1, Pd5 : Bi2, and Pd1 : Bi2, respectively). Larger clusters (with more atoms) will

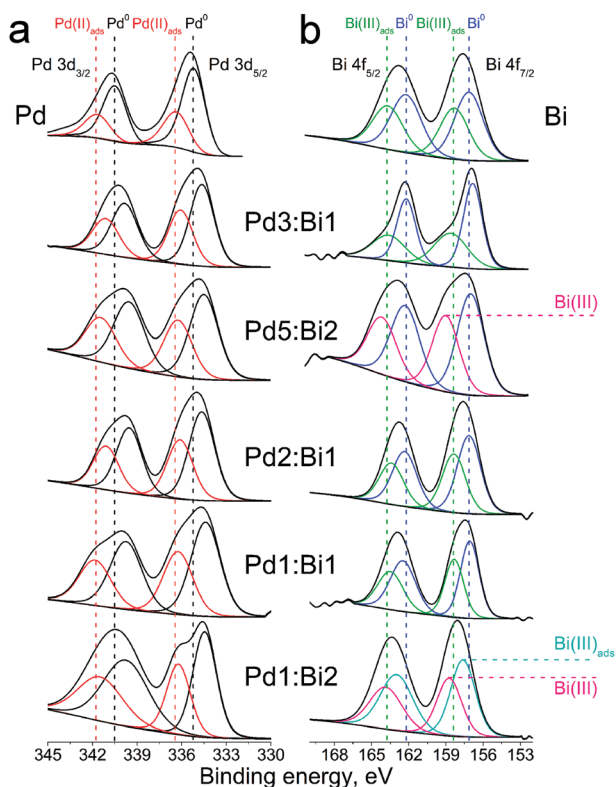


Fig. 3 X-ray photoelectron spectra of mono- and bimetallic catalysts for Pd 3d (a) and Bi 4f (b) levels.

possess a stronger screening effect and, as a consequence, lower binding energy.<sup>46</sup> A similar tendency was reported by Venezia *et al.* for the pumice-supported Pd–Pt system and by Koel *et al.* for Pd films deposited on Au.<sup>47,48</sup>

### Measurement of catalytic properties

The obtained catalyst samples were studied in the glucose oxidation to gluconic acid at a [Glu]:[Pd] molar ratio of 5000:1 (Fig. 4). In the presence of the Pd/Al<sub>2</sub>O<sub>3</sub> sample, the conversion is 29% (Table 3). Low values of glucose conversion are probably related to the fact that monometallic palladium is deactivated during glucose oxidation due to oxygen penetration into the upper layers of palladium, which decreases the number of active sites.<sup>49</sup>

At a bismuth content below 25% of the total atomic metal content (Pd3:Bi1 sample) glucose conversion increased almost twofold – up to 56.6%. A possible explanation for this was proposed by Besson.<sup>26</sup> During the reaction bismuth accepts the excess of supplied oxygen forming Bi<sub>2</sub>O<sub>3</sub> thus protecting palladium from oxidation. Meanwhile, palladium adsorbs hydrogen from glucose, which then interacts with the oxygen in Bi<sub>2</sub>O<sub>3</sub> forming H<sub>2</sub>O. After H<sub>2</sub>O desorption, the active sites of the catalyst return to their pristine state.

The Pd5:Bi2 sample showed similar conversions compared to the Pd3:Bi1 sample. This is probably because the atomic compositions are rather similar. Further bismuth content increase (Pd2:Bi1, Pd1:Bi1, and Pd1:Bi2 samples) leads to a decrease in conversion compared to Pd3:Bi1 and Pd5:Bi2 samples (47.5%, 42.1%, and 27.8%, respectively). Fig. 4 shows the glucose conversion *versus* time graph. Despite different glucose conversions, high selectivity values for the desired product (93–100%) were noted for each sample. The only by-product was found to be fructose in the presence of Pd, Pd5:Bi2, and Pd2:Bi1 samples, which is a structural isomer of glucose.

Accordingly, one can assume that it is the particle size that changes the catalytic activity. Thus, the most active are particles

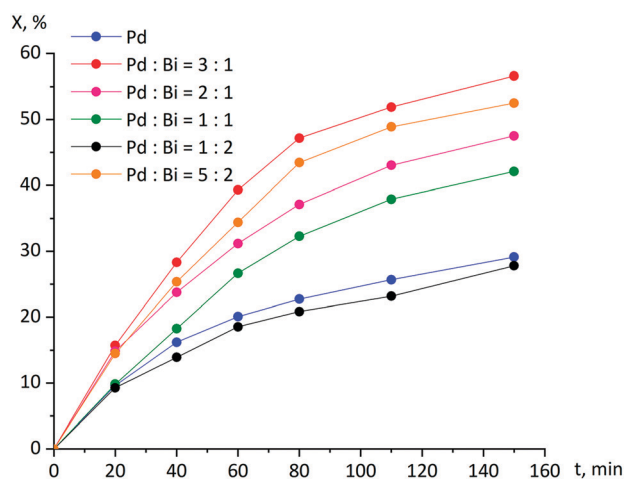


Fig. 4 Glucose conversion *versus* time in the presence of different catalysts.

Table 3 Quantitative characteristics for glucose oxidation reaction in the presence of Pdx:Bi<sub>y</sub>/Al<sub>2</sub>O<sub>3</sub> samples

Sample	X <sub>Glu</sub> , %	Y <sub>GluA</sub> , %	S <sub>GluA</sub> , %	TOF, s <sup>-1</sup>
Pd	29.1	27.1	93.1	0.46
Pd3:Bi1	56.6	56.6	>99.9	0.68
Pd5:Bi2	52.2	51.8	99.2	0.56
Pd2:Bi1	47.5	47.4	99.7	0.60
Pd1:Bi1	42.1	42.1	>99.9	0.43
Pd1:Bi2	27.8	27.8	>99.9	0.38

with a diameter varying in the range from 4 to 10 nm. Nanoparticles of this diameter are present in Pd3:Bi1, Pd5:Bi2, and Pd2:Bi1 samples, which demonstrated the highest glucose conversion and gluconic acid yield values. The lowest glucose conversion values were achieved in the presence of Pd1:Bi1 and Pd1:Bi2 samples, whose powders contain a significant amount of large particles formed due to the sintering of palladium with bismuth during heat treatment, when the amount of loaded bismuth was more than 50% of the total metal atomic loading.<sup>26</sup>

### Post-catalytic sample investigation

The samples were examined by XRF and XPS after catalytic tests. The catalyst samples were isolated from the reaction mixture after catalytic tests, washed with distilled water, and dried at room conditions. Since XRF determines the relative element content in the entire bulk of the clusters and XPS measures the element percentage only in the surface layer of the particle, significant differences in the data obtained with these two methods may be present.

The results of XRF analysis (Table 4) showed that samples with small particle sizes, typical of low-bismuth ( $\leq 25\%$  of total metal content) compositions, are less susceptible to leaching into the reaction medium.<sup>50</sup> For the Pd3:Bi1 sample, there is a  $\sim 6\%$  and  $\sim 4\%$  content decrease for palladium and bismuth, respectively. Particles with a larger bismuth content ( $\geq 50\%$ ) show substantial leaching (up to 65% palladium and 49% bismuth). This difference is caused by weaker binding of Bi-rich particles to the support due to the larger size and their lesser stability (see the 'Pd<sub>n</sub>Bi<sub>m</sub> cluster characterization' section). Such high bismuth loss with growing bismuth percentage for was reported by Wenkin Pd<sub>x</sub>:Bi<sub>y</sub>/C catalysts.<sup>51</sup>

XPS was used to measure the relative element content of the samples before and after catalytic tests (Table 5). The Pd5:Bi2 sample demonstrates the highest extent of bismuth leaching, which results in a significant Pd:Bi ratio change of 4.2.

Table 4 Palladium and bismuth content in Pdx:Bi<sub>y</sub>/Al<sub>2</sub>O<sub>3</sub> catalyst samples after catalytic tests

Sample	Pd content, wt%	Pd loss, %	Bi content, wt%	Bi loss, %
Pd3:Bi1	3.3	5.7	2.3	4.2
Pd5:Bi2	2.2	12.0	2.2	4.3
Pd2:Bi1	2.0	28.6	1.6	30.4
Pd1:Bi1	0.6	45.5	2.3	41.0
Pd1:Bi2	0.8	65.2	2.2	48.8

**Table 5** Element atomic percentage for obtained samples before and after catalytic tests

Sample		O, at%	Al, at%	Pd, at%	Bi, at%	Pd:Bi ratio
Pd3:Bi1	Before	53.10	44.75	1.46	0.69	2.11
	After	46.58	52.71	0.54	0.18	3.00
Pd5:Bi2	Before	47.31	51.87	0.50	0.32	1.56
	After	48.66	50.79	0.47	0.09	5.05
Pd2:Bi1	Before	53.49	45.73	0.38	0.41	0.93
	After	51.43	48.09	0.29	0.21	1.38
Pd1:Bi1	Before	51.34	47.59	0.37	0.70	0.53
	After	52.59	46.96	0.27	0.17	1.59
Pd1:Bi2	Before	50.94	47.56	0.30	1.20	0.25
	After	45.89	50.88	0.28	0.25	1.12

Bismuth content decrease mainly contributes to the change of Pd:Bi ratio with an exception for the Pd3:Bi1 sample. Actual Pd:Bi ratios before catalysis are 1.5–2.0 times lower than the desired ones. This difference is caused by the fact that bismuth atoms partially cover palladium thus preventing its detection by XPS.<sup>52,53</sup> This idea is supported by the fact that bismuth possess lower surface energy compared to palladium.<sup>54,55</sup> Higher surface energy causes palladium atoms to aggregate more intensively than bismuth atoms, which results in palladium cluster formation with a further deposition of bismuth on its surface. This is also confirmed by the Pd–Bi cluster structure prediction performed in this work and discussed below.

### Pd<sub>n</sub>Bi<sub>m</sub> cluster characterization

The experimental techniques described above give precious information about the catalytic performance of nanoparticles, but give little information about their structures. Such knowledge is important to understand the chemistry of catalytic processes at the atomistic level and can shed light on the

behavior of selectivity with varying Pd:Bi ratios. On the other hand, the theoretical studies on this subject are missing as well. To grasp the main structural features, we modelled the studied nanocatalysts by free Pd<sub>n</sub>Bi<sub>m</sub> nanoclusters with widely varied area of compositions ( $n \leq 20$ ,  $m \leq 15$ ). The feasibility of such a vast global optimization emerged only with the development of a variable-composition evolutionary nanocluster structure prediction method,<sup>29</sup> where clusters with different compositions are optimized in one shot by means of effective exchange of the structural information. A number of the most illustrative examples out of 300 globally optimized structures are shown in Fig. 5 and divided in four groups discussed below.

Fig. 5a demonstrates the structures with Pd:Bi ratios equal or nearly equal to those from the bulk phase diagram. We first note that these atomic arrangements have little in common with corresponding crystals. Two of them (Pd<sub>9</sub>Bi<sub>9</sub> and Pd<sub>16</sub>Bi<sub>8</sub>) have structures of a distorted bcc lattice, and another two (Pd<sub>12</sub>Bi<sub>5</sub> and Pd<sub>15</sub>Bi<sub>5</sub>) are based on the Pd<sub>13-x</sub>Bi<sub>x</sub> icosahedra. These two structural motifs give rise to most of the locally stable clusters as we'll see below. All structures can be found in the ESI,<sup>†</sup> Table S4.

As the nanoparticles are always thermodynamically unstable against growth, various criteria of relative, or local stability can be applied. The most widely used one is the positive value of minimum second-order finite difference. The latter is defined as

$$\Delta_{\min}^2(m,n) = \min\{\Delta_{\text{Pd}}^2(m,n), \Delta_{\text{Bi}}^2(m,n)\}$$

where

$$\Delta_{\text{Pd}}^2(m,n) = E(\text{Pd}_{m+1}\text{Bi}_n) + E(\text{Pd}_{m-1}\text{Bi}_n) - 2E(\text{Pd}_m\text{Bi}_n),$$

and likewise for  $\Delta_{\text{Bi}}^2(m,n)$ . Thus, a cluster is considered stable, or “magic”, if  $\Delta_{\min}^2(m,n) > 0$ . Another important criterion is

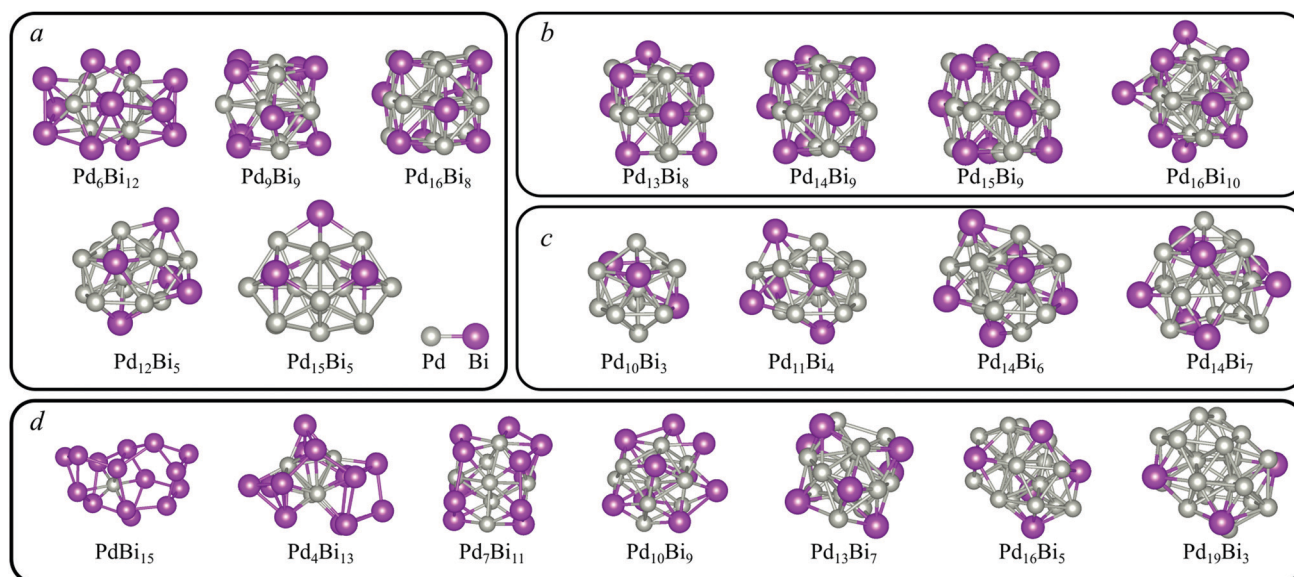


**Fig. 5** Structures of stable Pd<sub>m</sub>Bi<sub>n</sub> clusters: (a) having Pd:Bi ratios corresponding to stable compounds on the phase diagram; (b) based on bcc structural motif; (c) based on Pd<sub>x</sub>Bi<sub>13-x</sub> icosahedron; (d) showing that with a Pd:Bi decrease, Bi atoms tend to occupy ‘jewel’ positions changing to a Pd–Bi core–shell structure.



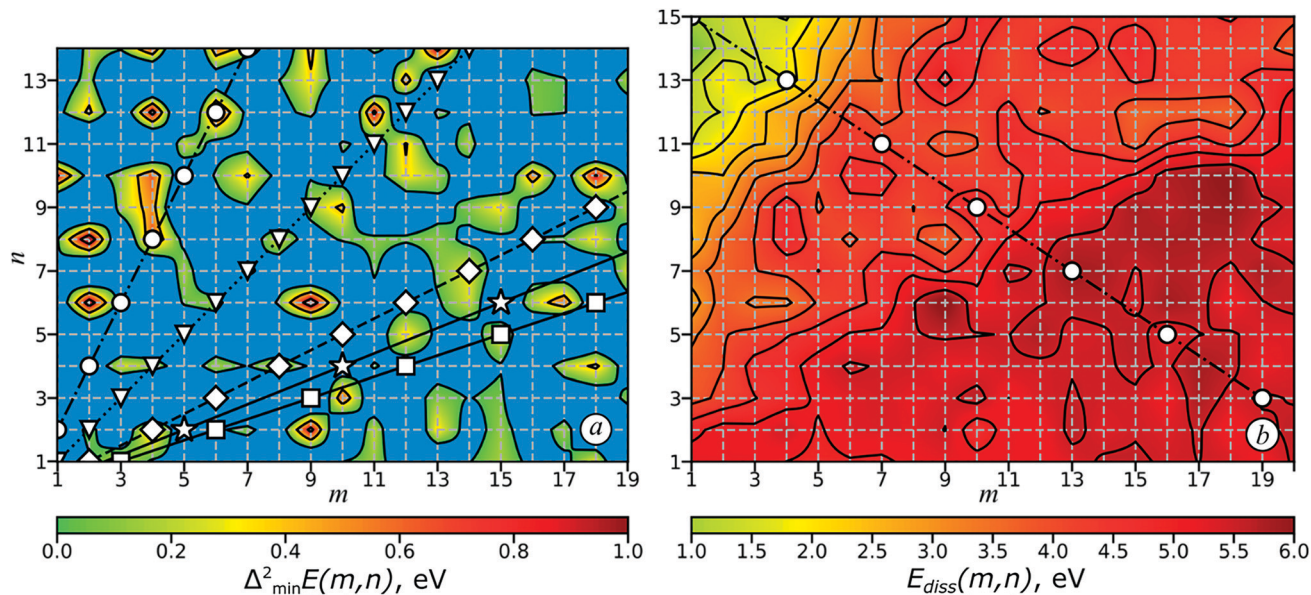


Fig. 6 Maps of stability in  $\text{Pd}_m\text{Bi}_n$  clusters according to two criteria: (a)  $\Delta_{\min}^2 E(m, n)$  (in eV) as a function of  $m$  and  $n$ , showing resistance to transfer of Pd or Bi atom between two identical clusters. Marked are Pd:Bi ratios from the bulk phase diagram (1:2 – circles, 1:1 – triangles, 5:2 – stars and 3:1 – squares). Regions of instability are marked in a blue color. (b)  $E_{\text{diss}}(m, n)$  showing resistance to dissociation into fragments. Marked are clusters with gradually varied Pd:Bi ratio.

based on minimal dissociation energy. For a given cluster,  $\text{Pd}_n\text{Bi}_m$ , all possible dissociations are considered and the minimum dissociation energy,  $E_{\text{diss}}(m, n)$ , is used as the degree of stability. These two measures of stability were calculated for all 300 compositions and mapped in  $m$ - $n$  coordinates in Fig. 6.

The map of  $\Delta_{\min}^2(m, n)$  in Fig. 6a has a few groups of ‘stability islands’. The example is the area of  $\text{Pd}_{9+x}\text{Bi}_{2+x}$  with  $x$  running from zero up to about 7. The corresponding structures are built either with bcc motif (Fig. 5b) or out of icosahedron (Fig. 5c). Interestingly, most of the stable nanoclusters have even numbers of Bi atoms – which renders the number of electrons in the whole cluster even (if the number of electrons were odd, we would have a magnetic cluster with open-shell electronic structure). In all cases the Bi atoms are always on the surface of the clusters and tend to form bonding with Pd rather than with Bi. We also plotted the lines corresponding to bulk compounds. It is seen, that contrary to our previous studies of ionic-covalent systems,<sup>29,56</sup> there is no correlation between the stability of crystalline and cluster compositions.

This, together with a rather disordered pattern of a map, might be attributed to the extreme complexity of intermetallic phase diagrams, especially at nanoscale sizes, where surface comes into play.

To examine the effect of Pd:Bi ratio on structure and stability let us look at the line  $\text{Pd}_{1+3x}\text{Bi}_{15-2x}$  going across the whole map of dissociation energy  $E_{\text{diss}}(m, n)$  (Fig. 6b). The corresponding structures are given in Fig. 5d.  $\text{Pd}_4\text{Bi}_{13}$  denotes the transition from clusters with Bi atoms having no Pd neighbors ( $\text{PdBi}_{15}$ ) to those where all Bi atoms are bound to Pd atoms ( $\text{Pd}_7\text{Bi}_{11}$ ). This transition is accompanied by an  $E_{\text{diss}}$  gain of about 3 eV.  $\text{Pd}_{10}\text{Bi}_9$  clusters turn from core-shell to crown-jewel geometry meaning that all Bi atoms are bound only

to surface Pd atoms. At the same time clusters become even more stable entering the area of  $E_{\text{diss}} \approx 6$  eV. These observations lead to a number of conclusions. The first one is already mentioned. Bismuth tends to form a shell, which is consistent with its lower surface energy compared to palladium, and typically lower coordination numbers of bismuth atoms. This can also be explained by the presence of lone electron pairs in Bi(III)-facing outwards. Second, low dissociation energies of Bi-rich clusters explain higher metal leaching into the reaction media. And most importantly, since promoting bismuth causes occupying of surface sites, its lower amount (compared to bulk) will benefit the reaction the most, since at a higher amount it tends to form a shell, which blocks the active Pd centers.

The performed calculations and catalytic tests are consistent with the scheme of oxidative dehydrogenation of glucose proposed by Besson *et al.* (Fig. 7).<sup>26</sup> Bismuth, which is deposited on the surface of a palladium nanocluster, has a higher affinity for oxygen than palladium.<sup>57</sup> In the presence of an oxidizing agent, bismuth undergoes oxidation itself, thus protecting the active sites of the palladium cluster from deactivation. Hydrogen chemisorbed on the palladium surface binds with oxygen chemisorbed by bismuth forming water and or hydrogen peroxide, which is desorbed from the surface afterwards. Simultaneously, a lactone formation occurs, which is then converted into gluconate ion in alkaline medium.

Thus, bismuth is predominantly oxidized in the course of the reaction, and the interaction of bismuth oxide with palladium hydride regenerates metallic bismuth in the catalytic cycle and prevents palladium oxidation.

Promotion of catalysts leads to an increase of their activity, as well as resistance to oxidative deactivation. An increase in the stability of a catalyst containing a noble metal such as

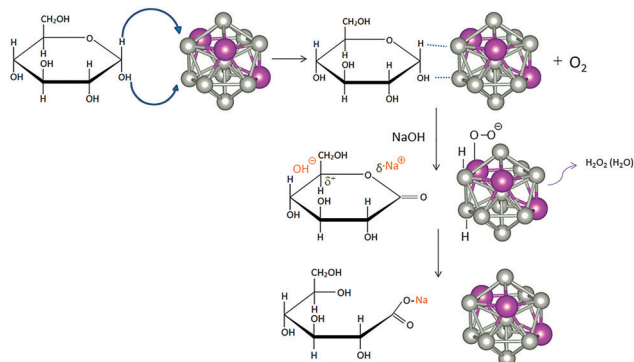


Fig. 7 Scheme of oxidative dehydrogenation of glucose on the surface of a Pd<sub>10</sub>Bi<sub>3</sub> nanocluster.

palladium with the addition of a non-noble metal such as bismuth, which is oxidized much more easily than the platinum group elements, indicates a synergistic effect. A noticeable decrease in catalytic activity in the presence of the Pd1:Bi2 catalyst is caused not only by the blockage of palladium atoms, but also due to the fact that the Bi<sup>0</sup> phase is absent, and bismuth is in the valence state Bi(III). Thus, bismuth is unable to adsorb oxygen and prevent oxidation of the catalytic surface.

## Conclusions

This investigation highlights the following points:

(I) Obtained mono- and bimetallic samples have an average particle size of 4–15 nm. Growing bismuth content leads to particle aggregation and enlargement causing weaker bonding with the support, which results in particles washing out.

(II) Palladium atoms are characterized by an excess of electron density for the Pd<sup>0</sup> state induced by bismuth's electron-donor influence, as follows from XPS patterns. The oxidized state of palladium Pd(II)<sub>ads</sub> is formed by strong interaction between palladium and alumina's oxygen atoms. Bismuth is located on the palladium atoms thus preventing their detection by XPS. At high bismuth content (Pd1:Bi1, Pd1:Bi2) bismuth completely turns into its oxidized state, which is possibly one of the reasons for its low catalytic activity.

(III) Pd<sub>x</sub>:Bi<sub>y</sub> clusters tend to form “crown-jewel” structures with bismuth atoms located on the palladium core, as shown by USPEX-code structure optimization. No apparent correlation between the cluster stability and metal ratio was found. The cluster's tendency for fragmentation increases with growing Bi-content resulting in greater metal losses. Calculations of Bader atomic charges demonstrate an excess of electron density on palladium atoms, which is consistent with XPS patterns.

(IV) The Pd<sub>3</sub>:Bi<sub>1</sub>/Al<sub>2</sub>O<sub>3</sub> sample demonstrated the highest activity (gluconic acid yield of ~57%). This atomic ratio grants the smallest particle size and the optimal coverage of palladium core by bismuth that protects active sites from oxidation and does not block them completely.

## Author contributions

M. P. Sandu – conceptualization, data curation, formal analysis, investigation, methodology, visualization, writing – original draft, writing – review & editing. M. A. Kovtunov – conceptualization, data curation, formal analysis, investigation, methodology, visualization, writing – original draft, writing – review & editing. V. S. Baturin – formal analysis, investigation, methodology, software, visualization, writing – original draft, writing – review & editing. A. R. Oganov – writing – review & editing, formal analysis, methodology, funding acquisition. I. A. Kurzina – project administration, resources, supervision, conceptualization, funding acquisition, writing – review & editing, visualization.

## Conflicts of interest

There are no conflicts to declare.

## Acknowledgements

This research was financially supported by the Competitiveness Improvement Program of National Research Tomsk State University (Grant No. 8.2.02.2020, 8.2.10.2018) and the Ministry of Science and Higher Education of the Russian Federation (Grant No. 2711.2020.2 to leading scientific schools).

## Notes and references

- 1 A. M. Canete-Rodriguez, I. M. Santos-Duenas, J. E. Jimenez-Hornero, A. Ehrenreich, W. Liebl and I. Garcia-Garcia, *Process Biochem.*, 2016, **51**, 1891–1903.
- 2 S. Ramachandran, P. Fontanille, A. Pandey and C. Larroche, *Food Technol. Biotechnol.*, 2006, **44**, 185–195.
- 3 F. Lu, K. Ping, L. Wen, W. Zhao, Z. Wang, J. Chu and Y. Zhuang, *Process Biochem.*, 2015, **50**, 1342–1348.
- 4 H. Zhang, J. Zhang and J. Bao, *Bioresour. Technol.*, 2016, **203**, 211–219.
- 5 M. B. Farhat, I. Boukhris and H. Chouayekh, *FEMS Microbiol. Lett.*, 2015, **362**, fmv008.
- 6 C. Hidalgo, E. Mateo, A. B. Cerezo, M. J. Torija and A. Mas, *Int. J. Wine Res.*, 2010, **2**, 5–61.
- 7 H. Hustede, H. Haberstroh and E. Schinzig, *Ullmann's Encyclopedia of Industrial Chemistry*, Wiley-VCH Verlag, Weinheim, 2000, pp. 37–43.
- 8 H. Znad, J. Markoš and V. Baleš, *Process Biochem.*, 2004, **39**, 1341–1345.
- 9 O. V. Singh and R. Kumar, *Appl. Microbiol. Biotechnol.*, 2007, **75**, 713–722.
- 10 S. Anastassiadis and I. G. Morgunov, *Recent Pat. Biotechnol.*, 2007, **1**, 167–180.
- 11 L. M. Harvey and B. McNeil, in *Aspergillus*, ed J. E. Smith, Springer, Boston, MA, 1st edn, 1994, ch. 6, pp. 141–176.
- 12 P. Qi, S. Chen, J. Chen, J. Zheng, X. Zheng and Y. Yuan, *ACS Catal.*, 2015, **5**, 2659–2670.



- 13 X. Liu, Y. Yang, S. Su and D. Yin, *Catal. Lett.*, 2017, **147**, 383–390.
- 14 C. Liu, J. Zhang, J. Huang, C. Zhang, F. Hong, Y. Zhou, G. Li and M. Haruta, *ChemSusChem*, 2017, **10**, 1976–1980.
- 15 M. Ali, M. Rahman, S. M. Sarkar and S. B. A. Hamid, *J. Nanomat.*, 2014, **2014**, 23.
- 16 M. Comotti, C. Della Pina and M. Rossi, *J. Mol. Catal. A: Chem.*, 2006, **251**, 89–92.
- 17 H. Zhang and N. Toshima, *Catal. Sci. Technol.*, 2013, **3**, 268–278.
- 18 P. N. Amaniampong, X. Jia, B. Wang, S. H. Mushrif, A. Borgna and Y. Yang, *Catal. Sci. Technol.*, 2015, **5**, 2393–2405.
- 19 H. Zhang, T. Watanabe, M. Okumura, M. Haruta and N. Toshima, *J. Catal.*, 2013, **305**, 7–18.
- 20 H. Zhang, J. Okuni and N. Toshima, *J. Colloid Interface Sci.*, 2011, **354**, 131–138.
- 21 D. L. Weissman-Wenocur and W. E. Spicer, *Surf. Sci.*, 1983, **133**, 499–515.
- 22 M. Wenkin, R. Touillaux, P. Ruiz, B. Delmon and M. Devillers, *Appl. Catal., A*, 1996, **148**, 181–199.
- 23 S. Karski, *J. Mol. Catal. A: Chem.*, 2006, **253**, 147–154.
- 24 I. Witońska, M. Frajtek and S. Karski, *Appl. Catal., A*, 2011, **401**, 73–82.
- 25 S. Karski, T. Paryjczak and I. Witońska, *Kinet. Catal.*, 2003, **44**, 618–622.
- 26 M. Besson, F. Lahmer, P. Gallezot, P. Fuertes and G. Fleche, *J. Catal.*, 1995, **152**, 116–121.
- 27 P. Fuertes and G. Fleche, *Eu. Pat.*, 0233816A1, 1987.
- 28 M. P. Sandu, V. S. Sidelnikov, A. A. Geraskin, A. V. Chernyavskii and I. A. Kurzina, *Catalysts*, 2020, **10**, 271.
- 29 S. V. Lepeshkin, V. S. Baturin, Y. A. Uspenskii and A. R. Oganov, *J. Phys. Chem. Lett.*, 2019, **10**, 102–106.
- 30 A. R. Oganov and C. W. Glass, *J. Chem. Phys.*, 2006, **124**, 244704.
- 31 A. R. Oganov, A. O. Lyakhov and M. Valle, *Acc. Chem. Res.*, 2011, **44**, 227–237.
- 32 P. E. Blöchl, *Phys. Rev. B: Condens. Matter Mater. Phys.*, 1994, **50**, 17953–17978.
- 33 J. P. Perdew, K. Burke and M. Ernzerhof, *Phys. Rev. Lett.*, 1996, **77**, 3865.
- 34 G. Kresse and J. Hafner, *Phys. Rev. B: Condens. Matter Mater. Phys.*, 1993, **47**, 558–561.
- 35 G. Kresse and J. Furthmüller, *Phys. Rev. B: Condens. Matter Mater. Phys.*, 1996, **54**, 11169–11186.
- 36 T. Lu and F. Chen, *J. Comput. Chem.*, 2012, **33**, 580–592.
- 37 Y. Wang and Y. Xia, *Nano Lett.*, 2004, **4**, 2047–2050.
- 38 M. C. Militello and S. J. Simko, *Surf. Sci. Spectra*, 1994, **3**, 387–394.
- 39 D. L. Mowery, M. S. Graboski, T. R. Ohno and R. L. McCormick, *Appl. Catal., B*, 1999, **21**, 157–169.
- 40 Y. Huang, Y. Zhang, H. Liu and Z. Gu, presented in part at the International Symposium on Photoelectronic Detection and Imaging 2011, Beijing, China, August, 2011.
- 41 B. Zhao, T. Chen, H. Pan, D. Fu and Y. Han, *Phys. E*, 2016, **78**, 79–84.
- 42 M. C. Valero, P. Raybaud and P. Sautet, *J. Catal.*, 2007, **247**, 339–355.
- 43 I. G. Casella and M. Contursi, *Electrochim. Acta*, 2006, **52**, 649–657.
- 44 I. Witońska, A. Królak and S. Karski, *J. Mol. Catal. A: Chem.*, 2010, **331**, 21–28.
- 45 S. Karski, *J. Mol. Catal. A: Chem.*, 2006, **253**, 147–154.
- 46 F. S. Roberts, S. L. Anderson, A. C. Reber and S. N. Khanna, *J. Phys. Chem. C*, 2015, **119**, 6033–6046.
- 47 A. M. Venezia, D. Duca, M. A. Floriano, G. Deganello and A. Rossi, *Surf. Interface Anal.*, 1992, **19**, 543–547.
- 48 B. E. Koel, A. Sellidj and M. T. Paffett, *Phys. Rev. B: Condens. Matter Mater. Phys.*, 1992, **46**, 7846.
- 49 I. Nikov and K. Paev, *Catal. Today*, 1995, **24**, 41–47.
- 50 D. Roth, P. Gelin, A. Kaddouri, E. Garbowski, M. Primet and E. Tena, *Catal. Today*, 2006, **112**, 134–138.
- 51 M. Wenkin, P. Ruiz and M. Devillers, *J. Mol. Catal. A: Chem.*, 2002, **180**, 141–159.
- 52 S. Vajíček, M. Štolcová, A. Kaszonyi, M. Mičušík, P. Alexy, P. Canton, G. Onyestyák, S. Harnos, F. Lónyi and J. Valyon, *J. Ind. Eng. Chem.*, 2016, **39**, 77–86.
- 53 M. Wenkin, C. Renard, P. Ruiz, B. Delmon and M. Devillers, *Stud. Surf. Sci. Catal.*, 1991, **110**, 517–526.
- 54 W. R. Tyson and W. A. Miller, *Surf. Sci.*, 1977, **62**, 267–276.
- 55 R. Tran, Z. Xu, B. Radhakrishnan, D. Winston, W. Sun, K. A. Persson and S. P. Ong, *Sci. Data*, 2016, **3**, 1–13.
- 56 V. Baturin, S. Lepeshkin, N. Bushlanova and Y. Uspenskii, *Phys. Chem. Chem. Phys.*, 2020, **22**, 26299–26305.
- 57 P. Gallezot, M. Besson and F. Fache., in *Catalysis of Organic Reactions*, ed. M. G. Scaros and M. L. Prunier, CRC Press, Boca Raton, FL, 1st edn, 2017, ch. 30, pp. 317–327.